GEOPHYSICS, VOL. 78, NO. 2 (MARCH-APRIL 2013); P. E67–E77, 11 FIGS.
10.1190/GEO2012-0112.1

Downloaded 02/11/13 to 62.92.124.145. Redistribution subject to SEG license or copyright; see Terms of Use at http://library.seg.org/

The marine controlled-source electromagnetic method in shallow water

Rune Mittet[1] and Jan Petter Morten[1]

ABSTRACT

We analyzed marine controlled-source electromagnetic (CSEM) acquisition in shallow water by analytic and numerical calculations. The problem at hand was the fact that the amplitude of the airwave due to a horizontal electric dipole becomes larger as the water depth is reduced. The amplitude of the scattered field from a buried thin resistor would be difficult to extract from the increased total field if the scattered-field amplitude were independent of water depth. However, we identified and explained a compensating effect where the amplitude of the scattered field increases with reduced water depth. This amplification effect makes marine CSEM surveys in shallow water feasible. We derived an approximate expression for the total field for a simple but realistic conductivity model. This expression explains why the amplitudes of the term that describes the background field contribution and the term that gives the scattered field from the thin resistor increase when the water depth is reduced. Our results and sensitivity analysis indicated that the sensitivity of marine CSEM data acquired in a water depth of 40 m is comparable to the sensitivity of marine CSEM data acquired in a water depth of 300 m.

INTRODUCTION

The marine controlled-source electromagnetic (CSEM) method was introduced as a technique to determine the high resistivity of the lithosphere in deep water. The purpose was to compensate for the low amplitudes of the magnetotelluric (MT) fields at high frequencies (Cox, 1980; Young and Cox, 1981). The signal contribution from interactions at the air-water interface (airwave) was of little concern in this case due to the large water depth, which attenuates any such signal when the source and receiver are near the seafloor. Issues related to the airwave attracted more attention when the marine CSEM method was introduced as a hydrocarbon exploration tool (Eidesmo et al., 2002; Ellingsrud et al., 2002). It would be an obvious limitation if the method could be used in deep water only, because many prospects are situated in shallow-water areas. An overview of the marine CSEM method and its development as a hydrocarbon exploration tool is given in Constable (2010).

The concern with regard to the airwave has been that when the transmitted waveform is a harmonic, the response from a resistive thin hydrocarbon-bearing layer can be hard to detect in shallow water areas because the airwave contribution increases when water depth decreases. Thus, 10 years ago, the view was that the marine CSEM method had problems in water depths of 500 m or less, and several papers have since suggested techniques to mitigate the airwave response (see, e.g., Andréis and MacGregor, 2008; Maaø and Nguyen, 2010; Chen and Alumbaugh, 2011).

The water depth dependence of the total field due to the airwave effect is demonstrated using field data in Figure 1. This plot shows normalized inline electric field data from a survey area close to the equator, where the water depth varied considerably. The data were measured by receivers deployed at different water depths, and the source was for each receiver towed close to the seafloor along constant water-depth contours. The indicated depths pertain to the actual water depth at the receiver positions. Slightly different source waveforms were used, and in the plot, the frequencies displayed are in the range 0.25 to 0.3 Hz. From these results, we can infer the typical total field dependence on the water depth. The total recorded field is the sum of several contributions including the airwave and potentially also the scattered field from a buried resistive hydrocarbon reservoir. Comparing to deep water (1841-m water depth), Figure 1 shows that the total field amplitude can be two times larger at a 352-m water depth at a source-receiver offset of less than 8000 m, and one to two orders of magnitude larger at a 45-m water depth. This is a challenge if the scattered field from a buried resistor has an amplitude that is independent of water depth. In particular, there are contributions to noise and uncertainty that scale with the amplitude of the total recorded field. If these contributions are of the same size as the scattered field we seek, then the identification of the scattered field response becomes very hard.

Manuscript received by the Editor 30 March 2012; revised manuscript received 21 August 2012; published online 4 February 2013.
[1]Electromagnetic Geoservices (EMGS), Trondheim, Norway. E-mail: rm@emgs.com; jpmorten@emgs.com.
© 2013 Society of Exploration Geophysicists. All rights reserved.

Downloaded 02/11/13 to 62.92.124.145. Redistribution subject to SEG license or copyright; see Terms of Use at http://library.seg.org/

It was clear by 2003 that marine CSEM could be applied successfully in water depths of 300 m. Work with synthetic data indicated that frequency-domain marine CSEM combined with up-down decomposition (Amundsen et al., 2006) gave sufficient sensitivity to a buried resistor at these water depths. This was part of the motivation for the first calibration survey on the Troll Western Gas Province in 2003 (Johansen et al., 2005), where the water depth is approximately 330 m. In fact, it turned out that the response from the reservoir was so strong that up-down decomposition was not necessary to detect the reservoir. But, as demonstrated in Amundsen et al. (2006), the up-down decomposition enhanced the sensitivity to the hydrocarbon charged reservoir significantly when considering normalized amplitude and phase difference. A water depth of 300 m is not viewed as shallow water for marine CSEM surveys today. But what about water depths of 100 m or less?

In this paper, we will investigate the effect of reducing the water depth on the CSEM data analytically and by studying synthetic and real data. First, we will establish a measure that allows us to quantitatively compare the sensitivity to a buried thin resistor for different water depths. This shows that the sensitivity for, e.g., 300-m water depth is similar to 40-m water depth. Next, we derive an analytic expression for the CSEM response. The resulting expression explains quantitatively and qualitatively the dependence on water depth for the buried resistor response and the airwave. Finally, we study modeling results to further explore the shallow-water phenomenology.

SENSITIVITY OF CSEM IN SHALLOW WATER

In the introduction, we stated that the CSEM method is feasible in a 300-m water depth, and we raised the question of sensitivity at shallower water depths such as 100 m. Let us indicate the answer to this question from results of full waveform simulations, by which we define a modeling approach without other assumptions than a 1D model geometry (Løseth and Ursin, 2007). We associate sensitivity with the magnitude of the data difference between a simulation in which the model has a thin resistive layer (hydrocarbon reservoir) embedded (case A) and a simulation in which the background is the same but the resistive layer is absent (case B). We consider the x-directed electric field measurement from a receiver at position $\mathbf{r}_r$ due to a horizontal electric dipole along the x-direction with frequency f, angular frequency $\omega = 2\pi f$, at position $\mathbf{r}_s$ (inline data). This will be denoted $E_x(\mathbf{r}_r|\mathbf{r}_s, \omega)$. We can then define the complex data difference, or scattered field, as

$$\Delta E_x(\mathbf{r}_r|\mathbf{r}_s, \omega) = E_x^A(\mathbf{r}_r|\mathbf{r}_s, \omega) - E_x^B(\mathbf{r}_r|\mathbf{r}_s, \omega). \quad (1)$$

Finally, we include the effect of measurement inaccuracy by normalizing $\Delta E_x(\mathbf{r}_r|\mathbf{r}_s, \omega)$ to the estimated measurement uncertainty $\delta E_x(\mathbf{r}_r|\mathbf{r}_s, \omega)$ and we define the following quantity as a measure of sensitivity:

$$\Psi(\mathbf{r}_r|\mathbf{r}_s, \omega) = \left| \frac{\Delta E_x(\mathbf{r}_r|\mathbf{r}_s, \omega)}{\delta E_x(\mathbf{r}_r|\mathbf{r}_s, \omega)} \right|. \quad (2)$$

When the scattered field exceeds the uncertainty estimate, the sensitivity measure will be larger than unity $\Psi > 1$. This can also be seen as a minimum criterion that the target effect on the data sample is significant and detectable.

The measurement uncertainty can be estimated using error propagation analysis. This formalism allows us to take into account the partial contributions to uncertainty due to inaccurate information about, e.g., equipment positioning and calibration, as well as ambient noise. The predicted measurement uncertainty assuming independent and random contributions is given by the following expression:

$$\delta E_x(\mathbf{r}_r|\mathbf{r}_s, \omega) = \sqrt{\sum_n \left| \frac{\partial E_x(\mathbf{r}_r|\mathbf{r}_s, \omega)}{\partial p_n} \delta p_n \right|^2}. \quad (3)$$

Here, p_n denotes an experimental parameter with the associated measurement uncertainty δp_n. This could be, e.g., the transmitter position $\mathbf{r}_s$, that for some water depth was known only to an accuracy of 10 m.

In this study, we will use a simplified model to estimate the uncertainty due to positioning and calibration and assume that for these contributions $(\partial E_x/\partial p_n)\delta p_n \propto E_x$. It can be shown using detailed analysis (Mittet and Morten, 2012) that this is a good approximation for the offsets relevant in this paper. The approximate uncertainty model based on equation 3 to be used then becomes

$$\delta E_x(\mathbf{r}_s|\mathbf{r}_s, \omega) = \sqrt{|\alpha E_x^A(\mathbf{r}_r|\mathbf{r}_s, \omega)|^2 + \mathcal{N}^2}. \quad (4)$$

Here, we introduced the relative uncertainty in the field amplitude α. In this paper, we will use $\alpha \approx 3\%$ as a constant with respect to offset. The ambient noise contributions are captured by the water-depth-dependent term $\mathcal{N}$.

The ambient noise level can be much larger in shallow water than in deep water due to the less effective screening by the water layer. The noise sources could be MT signals or swell noise. In addition, we expect motion noise to increase when the water depth is reduced. There are also water-depth-independent contributions such as receiver self-noise. We have chosen some typical values relevant for normalized electric data:

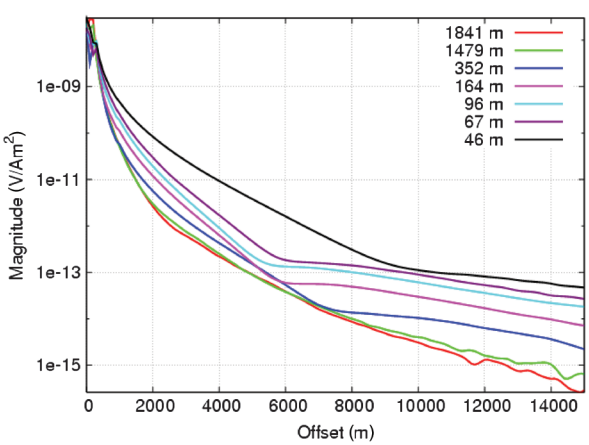

Figure 1. Real data amplitude from a survey area covering a wide range of water depths. For the different receivers, the displayed frequency is 0.25 Hz for water depths 1841 and 1479 m and 0.3 Hz for the other water depths shown.

Downloaded 02/11/13 to 62.92.124.145. Redistribution subject to SEG license or copyright; see Terms of Use at http://library.seg.org/

$$\mathcal{N}(2000\ \mathrm{m}) = 5\times10^{-16}\,\frac{\mathrm{V}}{\mathrm{Am}^2},$$
$$\mathcal{N}(300\ \mathrm{m}) = 3\times10^{-15}\,\frac{\mathrm{V}}{\mathrm{Am}^2},$$
$$\mathcal{N}(100\ \mathrm{m}) = 7\times10^{-15}\,\frac{\mathrm{V}}{\mathrm{Am}^2},$$
$$\mathcal{N}(40\ \mathrm{m}) = 1.5\times10^{-14}\,\frac{\mathrm{V}}{\mathrm{Am}^2}. \tag{5}$$

In Figure 2, we show the sensitivity defined by equation 2 and the uncertainty model described above for water depths ranging from deep (2000 m) to very shallow (40 m). The 1D conductivity model is shown in Figure 3. From Figure 2, we see that the sensitivity to the target is expected to be good for all water depths because it by far exceeds the threshold $\Psi = 1$ for a wide offset range. Furthermore, we can expect that the sensitivity will be reduced when the water depth is decreased from 2000 to 300 m, but further reduction of the water depth gives an insignificant effect on sensitivity. Because extensive experience has established that the CSEM method works well at, e.g., a 300-m water depth (for some recent examples, see, e.g., Fanavoll et al., 2012), we can therefore expect that similar targets can be characterized equally well at shallower water depths. Indeed, CSEM data are today routinely acquired in water depths of less than 100 m. Several surveys have been performed in water depths of 40 to 50 m. Data acquired at these water depths are processed in a standard manner by 3D inversion. No special preprocessing of the data is required.

We will take a broad definition of the term *airwave*, which in the following discussions will refer to any signal arising due to interactions with the air-water interface. The airwave amplitude will be governed by attenuation of the electromagnetic signal propagating in the water column from the source close to the seafloor, up to the air-water interface, and back down to the receiver on the seafloor. We also need to take into account multiple reflections at the air-water and seabed interfaces.

The background model contribution due to the airwave and the response due to a resistive anomaly increase when the water depth is reduced. The increase in the amplitude of the scattered field from a buried resistor when the water depth is reduced is demonstrated in Mittet (2008). This effect does, to a large degree, compensate for the growth in the background model airwave amplitude with reduced water depth, and it makes frequency domain marine CSEM also feasible in very shallow water, that is, down to 40 m or even less.

We will derive an analytic expression that explains how the scattered field amplitude is influenced by the model parameters. Specifically, our calculation reveals that the scattered field amplification with decreased water depth is determined only by propagation effects in the background model. The relative scattered field amplification for different water depths d_1 and d_2, $\Delta E_x^{d_1}/\Delta E_x^{d_2}$, is thus independent of the target thickness and resistivity within the validity of the approximations. This ratio is determined only by the background models and the target burial depth. The analytic expression for the response further allows a phenomenological understanding of shallow-water interaction effects that we explore.

THEORY

In this section, we will first discuss the relative magnitude of the airwave and the scattered fields as a function of water depth. We then study the response analytically. The reason to derive the analytic expression is to expose the physics and phenomenology of the airwave and the interaction that enhances scattered fields in shallow water; i.e., the numerical solution of the forward modeling problem for the simple geometry studied is not the main point. Modeling codes that can tackle arbitrary 3D geometries exist and are more relevant in context of the numerical modeling problem.

For the rest of the paper, we will work with the model shown in Figure 3. The air conductivity is set to zero. The water conductivity is 3.2 S/m, the formation conductivity is 0.5 S/m, and the resistor conductivity is 0.01 S/m. The water depth is varied, and for the examples shown here, we will use water depths of 40, 100, 300, and 2000 m. The distance from the seabed to the top of the resistor

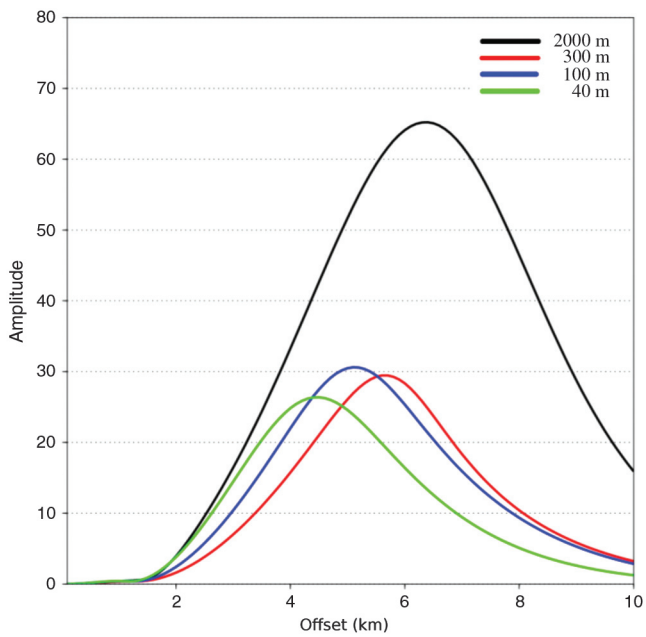

Figure 2. CSEM thin resistive layer sensitivity as a function of source-receiver offset. Sensitivity is measured as the magnitude of data difference to measurement uncertainty, defined in equation 2. The different curves show the sensitivity at different water depths. The frequency is 0.25 Hz, and the resistivity model is shown in Figure 3.

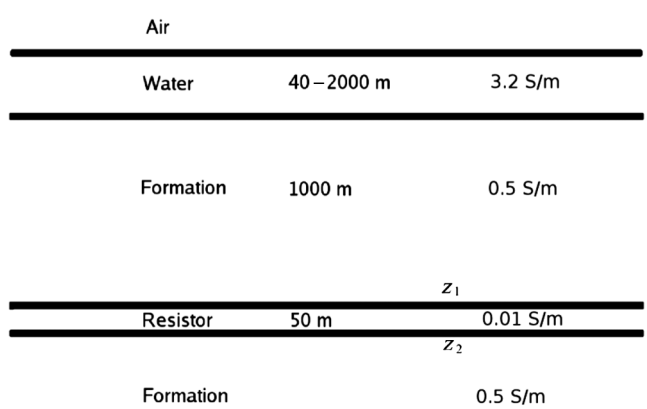

Figure 3. The model used for the analysis of the response from a thin resistive layer embedded in a conductive background medium.

Downloaded 02/11/13 to 62.92.124.145. Redistribution subject to SEG license or copyright; see Terms of Use at http://library.seg.org/

is 1000 m, and the resistor is 50 m thick. The receiver is positioned at the seabed, and the transmitter has an elevation above the seabed of 30 m for all examples. The color coding for the curves in all figures will be the same: green for 40-m water depth, blue for 100-m water depth, red for 300-m water depth, and black for 2000-m water depth.

We have already discussed how the background field amplitude increases when the water depth is decreased in relation to Figure 1. Let us now consider the scattered field from a buried resistor. The effect pointed to in Mittet (2008) that the increase in background signal amplitude with reduced water depth is accompanied with a corresponding increase in buried resistor scattered field, is shown in Figure 4. The curves show the absolute value of the inline electric difference field $|\Delta E_x(\mathbf{r}_r|\mathbf{r}_s)|$, defined in equation 1. The frequency is 0.25 Hz. The figure shows that the amplitude of the scattered field is much larger in the shallow-water cases (40 and 100 m) compared to the intermediate water depth case of 300 m and the deep-water case of 2000 m. For the 40-m water depth case, we observe that the scattered field is one order of magnitude larger than for the corresponding deep-water case. The effects observed here are not specific to a particular resistor burial depth. Furthermore, the demonstrated increase of the scattered field is also typical for other frequencies or subsurface resistivities that are commonly encountered in marine CSEM surveys. The one order of magnitude increase of the scattered field in shallow water is comparable to the amplitude increase of the background field discussed in relation to Figure 1 in the "Introduction."

We have now established quantitatively how much the airwave and scattered field amplitudes increase with decreasing water depth. That the scattered field also increases is important for the feasibility of CSEM in shallow water. To further understand the relative importance of the airwave and the scattered field as a function of water depth, we will now consider an analytic expression for the response from a thin resistive layer in a plane-layer model, Figure 3. The

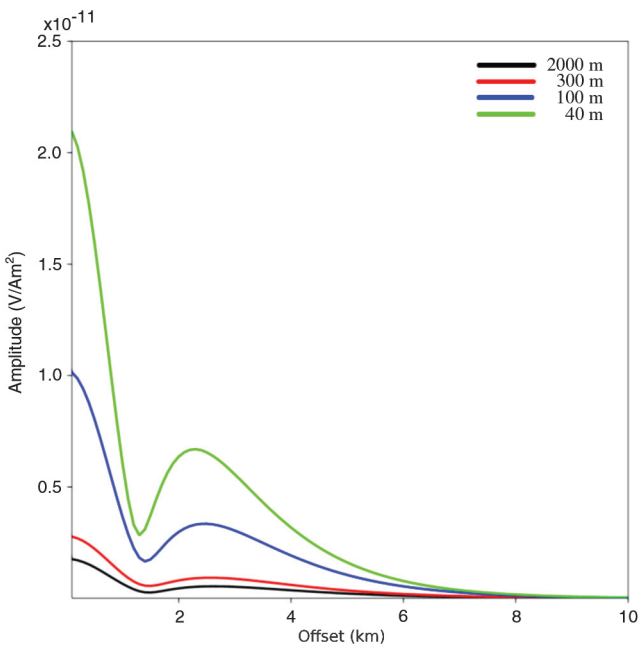

Figure 4. Absolute value of scattered fields calculated with a full waveform plane layer modeling scheme.

angular frequency argument ω is implicit in the following. We seek an expression for the inline electric field at the receiver position. This can be obtained from the electric Green's function, which is defined by the relation $E_x(\mathbf{r}_r|\mathbf{r}_s) = G^{EJ}_{xx}(\mathbf{r}_r|\mathbf{r}_s)p_x$, where $\mathbf{p} = p_x\hat{\mathbf{x}}$ is the dipole moment and $\hat{\mathbf{x}}$ is a unit vector in the x-direction. In the following, we consider normalized data equivalent to a unit source $p_x = 1$ Am. Thus, the numerical value of the electric field E_x and the Green's function component G_{xx} will coincide in magnitude, but have different units. The EJ superscript indicates that we consider an electric field due to an electric dipole source. The superscript HJ will be used to indicate a magnetic field due to an electric dipole source. The ij subscript indicate transmitting in the j direction and recording in the i direction. The Green's function is determined by frequency domain integral equations of the Lippmann-Schwinger type for the electric and magnetic Green's functions (Ward and Hohmann, 1987):

$$G^{EJ}_{kj}(\mathbf{r}_r|\mathbf{r}_s) = G^{B^{EJ}}_{kj}(\mathbf{r}_r|\mathbf{r}_s) + \int_{V_r} d\mathbf{r} G^{B^{EJ}}_{kl}(\mathbf{r}_r|\mathbf{r})\Delta\sigma_{li}(\mathbf{r})G^{EJ}_{ij}(\mathbf{r}|\mathbf{r}_s). \quad (6)$$

In this equation, the background electric Green's function components $G^{B^{EJ}}_{ij}$ will be evaluated from reflection series computations in the Fourier spatial wavenumber domain. The background here corresponds to the model without the anomalous resistive layer. The conductivity difference in the anomalous domain V_r is $\Delta\sigma_{nm}(\mathbf{r}) = \sigma^r_{nm}(\mathbf{r}) - \sigma^f_{nm}(\mathbf{r})$, where the superscript r is for the resistor and the superscript f is for the formation. The electric Green's tensor $G^{EJ}_{ij}(\mathbf{r}|\mathbf{r}_s)$ in the resistive anomalous domain ($\mathbf{r} \in V_r$) will be determined by an equation analogous to equation 6, where the arbitrary coordinate $\mathbf{r}_r$ is evaluated inside the anomalous resistive region.

Equation 6 is an integral equation in the space-frequency domain. Numerical solutions of these types of equations are discussed in Hohmann (1975), Weidelt (1975), and Zhdanov et al. (2006). Here we will make some simplifying assumptions to arrive at an analytic expression for this Green's function in the frequency-wavenumber domain. The derivation of expressions for background and anomalous domain Green's functions are in Appendix A. When these Green's functions are known, equation 6 becomes a straightforward integral over known fields, which is also discussed in Appendix A. Our main assumptions will be that the horizontal electric field component is negligible with respect to the vertical component inside the anomalous domain V_r (Brown et al., 2012). This assumption can be easily verified by full waveform modeling (Figure A-1 in Appendix A), and it is caused by the discontinuity of the vertical electric field as the conductivity changes from σ^f to σ^r. Moreover, the conductivity in the 1D model is assumed isotropic. Anisotropy can change the shallow-water amplitude-gain effect, but not by much compared to what is observed in Figure 4 for typical backgrounds.

Our calculations will be presented in the wavenumber-frequency domain, which is related to the space-frequency domain by the inverse Fourier transform

$$f(\mathbf{r}_h, z) = \frac{1}{(2\pi)^2}\int_{-\infty}^{\infty} d\mathbf{k}_h f(\mathbf{k}_h, z)e^{i\mathbf{k}_h\cdot\mathbf{r}_h}, \quad (7)$$

Downloaded 02/11/13 to 62.92.124.145. Redistribution subject to SEG license or copyright; see Terms of Use at http://library.seg.org/

where the horizontal wavevector is $\mathbf{k}_h = (k_x, k_y)$ and the horizontal coordinate vector is $\mathbf{r}_h = (x, y)$, where, e.g., $x = x_r - x_s$. The plotted results have been numerically transformed to the space-frequency domain.

The resulting expression for the recorded field at the receiver is derived in Appendix A (equation A-31) and can be expressed as

$$G_{xx}^{EJ}(\mathbf{k}_h, z_r|z_s) = G_{xx}^{B^{EJ}}(\mathbf{k}_h, z_r|z_s) + \Delta G_{xx}^{EJ}(\mathbf{k}_h, z_r|z_s). \quad (8)$$

This expression shows how the response can be represented as two separate contributions. The term $G_{xx}^{B^{EJ}}$ is independent of the resistor, and it describes the background response due to direct propagation as well as scattered and refracted signal associated with the air and formation. This contribution will include transverse electric (TE) and transverse magnetic (TM) components. The TE component is characterized by a vanishing vertical electrical field amplitude E_z (Ward and Hohmann, 1987). Such components do not generate a thin resistor response because that process requires that $E_z \neq 0$ at the resistor depth. However, at the long source-receiver offset, the TE component will dominate. This is because the TE mode can propagate with little attenuation and at high velocity through air (Løseth, 2011). The scattered field from the resistive anomaly is contained in ΔG_{xx}^{EJ},

$$\Delta G_{xx}^{EJ}(\mathbf{k}_h, z_r|z_s) = G_{xz}^{B^{EJ}}(\mathbf{k}_h, z_r|z_1)\frac{\eta}{1-\eta F_{zz}^{f^{EJ}}(\mathbf{k}_h)}G_{zx}^{B^{EJ}}(\mathbf{k}_h, z_1|z_s). \quad (9)$$

The background Green's functions $G_{xx}^{B^{EJ}}$, $G_{xz}^{B^{EJ}}$, and $G_{zx}^{B^{EJ}}$ that appear in equations 8 and 9 are given in Appendix A. The middle factor on the right hand side of equation 9 provides a coupling to the resistor. We defined $\eta = \Delta z \Delta\sigma\sigma^f/\sigma^r$, where $\Delta z = z_2 - z_1$ is the resistor thickness and

$$F_{zz}^{f^{EJ}}(\mathbf{k}_h) = \frac{1}{\sigma^f}\left(\frac{k_h^2}{-2ik_z^f}\right). \quad (10)$$

The wave-vector components are related by $k_z^f = \sqrt{k_\omega^2 - k_h^2}$, where $k_\omega^2 = i\mu\sigma^f\omega$ and μ denotes the magnetic permeability.

Equation 9 is the desired analytic expression for the buried resistor response. When we compare ΔG_{xx}^{EJ} to the expression for $G_{xx}^{B^{EJ}}$, we can determine the relative amplitude increase in resistor response and background response from reducing the water depth. The background Green's function $G_{xx}^{B^{EJ}}$ depends on the water depth and conductivities of the water and formation. The scattered field ΔG_{xx}^{EJ} additionally depends on the conductivity of the resistor and the distance from the seabed to the top resistor, as well as the resistor thickness. Equation 9 is an approximation for the full waveform expression given in equation 1.

We observe that if there is a gain in amplitude of the scattered field as the water depth decreases, then this effect must come from changes in $G_{zx}^{B^{EJ}}$ and $G_{xz}^{B^{EJ}}$. In equation 9, the middle factor giving the scattering amplitude is independent of the water depth. Only the Green's functions for downward ($G_{zx}^{B^{EJ}}$) and upward ($G_{xz}^{B^{EJ}}$) propagation depend on water depth.

Our interpretation of the increase in the scattered field response, in light of equation 9, is that the radiation pattern from an electric dipole is altered in shallow water in such a way that the vertical electric field in the formation is substantially increased. This increased vertical field (G_{zx}^{EJ}) couples to the resistor and creates the partially guided field. By reciprocity there will be a similar effect on the electromagnetic field propagating from the resistor to the receiver. Because the coupling to the resistor is via Green's functions with a nonzero vertical electrical field component ($G_{xz}^{B^{EJ}}$ and $G_{zx}^{B^{EJ}}$), this can be considered as a TM mode (Ward and Hohmann, 1987). The coupling to the resistor via nonzero vertical electric field components then identifies the airwave TM component as the cause for the shallow-water increased scattered field.

The TM mode of the airwave that is shown to interact in equation 9 can, due to the dependence on the reflection coefficients, be interpreted as raylike reflections at the air-water interface (Løseth, 2011) in combination with coupling to the thin resistor. Although the TE mode of the airwave does not contribute to the scattered field, it will have a dominant effect on far-offset data as mentioned above. These behaviors can also be demonstrated from the offset dependence of the gradient of the Green's function phase, which is related to propagation velocity. The phase curve for $G_{xx}^{B^{EJ}}$ will have a small gradient for intermediate and large source receiver offsets in shallow water. This is an indication of a very high propagation velocity, and it is due to the fact that a dominant contribution to the signal propagates through air. In the same offset range, the phase curve for $G_{zx}^{B^{EJ}}$ has a steep gradient. This indicates a relatively low propagation velocity, i.e., contrary to what we see for $G_{xx}^{B^{EJ}}$. Our interpretation is that propagation in the air layer is a negligible or nonexisting effect for $G_{zx}^{B^{EJ}}$.

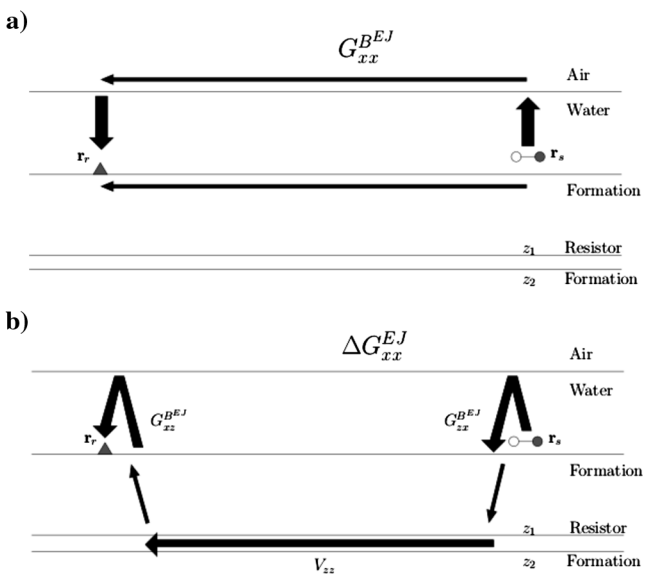

Figure 5. Schematic shallow-water CSEM signal propagation for the two terms contributing in equation 8. Thick arrows represent propagation by multiple reflections (between air-water and water-formation interfaces, or internally in the resistor), and thin arrows represent propagation also present in deep water. (a) The main airwave background contribution to $G_{xx}^{B^{EJ}}$ is governed by propagation along the air-water interface, and it constitutes a TE mode. An additional contribution is due to propagation along the water-formation interface. (b) The scattered field ΔG_{xx}^{EJ} is enhanced by signals arising due to interactions with the air-water interface. The Green's functions in equation 9, $G_{zx}^{B^{EJ}}$ and $G_{zx}^{B^{EJ}}$, correspond to downgoing and upgoing propagation, with interaction and propagation at the resistor described by $V_{zz} = \eta/(1-\eta F_{zz}^{f^{EJ}})$.

Downloaded 02/11/13 to 62.92.124.145. Redistribution subject to SEG license or copyright; see Terms of Use at http://library.seg.org/

The phenomenology of the terms contributing in equation 8 are conceptually illustrated in Figure 5. The main contribution to $G_{xx}^{B^{EJ}}$ from the airwave is characterized by propagation along the air-water interface, and it does not couple to the resistor because it is TE (Figure 5a). Interactions at the air-water interface also generate an enhanced downgoing propagation at a small distance from the source, which can couple to the resistor because it is TM ($E_z \neq 0$). There is a similar enhancement of the signal at the receiver location.

The scattered field in equation 9 can be simplified if the water layer is assumed to be sufficiently thick:

$$\Delta G_{xx}^{EJ}(\mathbf{k}_h, z_r|z_s) = -\frac{1}{4}\frac{\Delta\rho\Delta z k_x^2}{\left(1 + i\frac{\Delta\rho\Delta z}{\rho^f}\frac{k_h^2}{2k_z^f}\right)} \times (t_{TM}^{fw})^2 e^{ik_z^f(z_1-z_r)} e^{ik_z^f(z_1-z_w)} e^{ik_z^w(z_w-z_s)}. \tag{11}$$

The resistivity difference is $\Delta\rho = \rho^r - \rho^f$, where ρ^r and ρ^f are the resistor and formation resistivities, respectively. Equation 11 demonstrates that the response from the thin resistive layer has the property that the amplitude depends on the product, $\Delta\rho\Delta z$. This is in agreement with the transverse resistance equivalence discussed, e.g., by Constable and Weiss (2006) for $\rho^r \gg \rho^f$.

RESULTS

In this section, we will explore the predictions and the phenomenology inferred from the analytic results by numerical examples, where we use the full waveform modeling code.

Our result for the scattered field response, equation 9, is factorized such that the interaction with the resistive layer is contained in a single factor. This factor is independent of water depth. The background Green's functions that describe upward and downward propagation, on the other hand, depend on water depth but not on properties of the resistive layer. The factorization in equation 9 thus implies that the water depth dependence of the sensitivity defined by equation 2 depends on the resistive layer properties only as an overall scaling factor.

The absolute value of the downgoing field at resistor depth $G_{zx}^{B^{EJ}}$ is shown in Figure 6, and Figure 7 shows the same data normalized to the deep-water case. As we observe, the vertical field at the resistor depth is increased with a factor of up to four for the shallow-water case compared with the deep-water case. The increase is largest at small horizontal distances from the source. Thus, the most important contribution to the coupling of the source field with the thin resistor is at short horizontal distances. We will investigate this in more detail below. The increase in the vertical electric field will result in a larger guided field in the resistor through the middle factor in equation 9 that represents propagation in the resistive layer. Note that horizontal propagation between source and receiver will be dominated by this factor and not the distance-dependence of $G_{zx}^{B^{EJ}}$ shown in Figure 6. However, Figure 7 explains only part of the effect because we also need to consider the upgoing field $G_{xz}^{B^{EJ}}$ in equation 9. There will be a similar amplification with a factor of four for this propagation as the water depth is decreased. Equation 9 will be a double convolution in the space domain according to the transformation in equation 7. Decreasing the water depth from our deep-water case to the shallow-water case, the scattered field may thus be amplified by a factor that is up to 16, and this is consistent with what we observe in Figure 4.

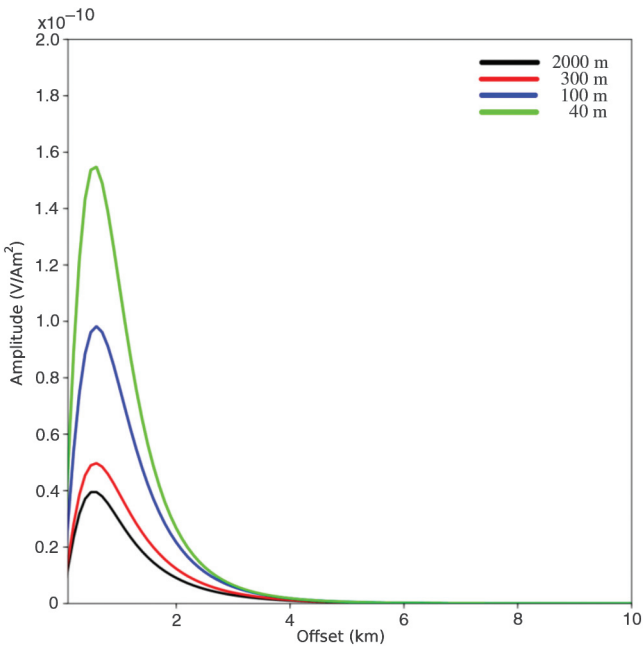

Figure 6. Vertical electric field magnitude from a horizontal electric dipole at the top of the resistor $|G_{zx}^{B^{EJ}}(\mathbf{r}_h, z_1|\mathbf{r}_s)|$. Note that the horizontal axis shows the lateral displacement from the source, and not the source-receiver offset. The field magnitude is plotted for the different water depths considered in the main text.

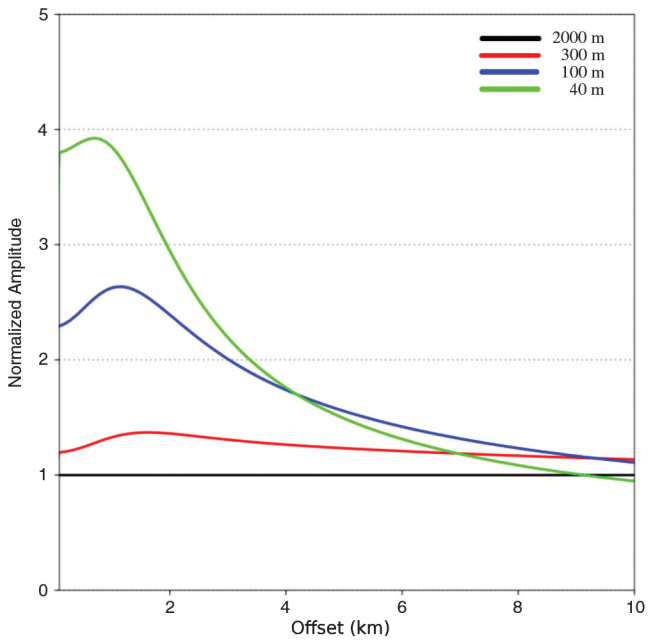

Figure 7. Vertical electric field magnitude from a horizontal electric dipole at the top of the resistor, normalized to the deep-water case. See also Figure 6. For short displacements from the source, the increase in field strength from deep to shallow water is up to four times.

Downloaded 02/11/13 to 62.92.124.145. Redistribution subject to SEG license or copyright; see Terms of Use at http://library.seg.org/

To analyze the sensitivity, the amplification of the background field $G_{xx}^{B^{EJ}}$ must be considered together with the amplification of the scattered field ΔG_{xx}^{EJ}. As described by equations 2 and 4, background field contributions affect sensitivity because there are contributions to the uncertainty that scale with the total field amplitude. We expect the TE mode of the airwave to give an important background field contribution because it does not couple to the resistor and can propagate with reduced attenuation in air (Løseth, 2011). This contribution is contained in the background field term in equation 8, $G_{xx}^{B^{EJ}}$. In Figure 8, we plot the background field together with the scattered field ΔG_{xx}^{EJ}. The solid lines are for $G_{xx}^{B^{EJ}}$, and the dashed lines are for ΔG_{xx}^{EJ}. There is an increase in the airwave amplitude as the water depth is reduced, but there is also a corresponding increase in the scattered field. The real data shown in Figure 1 show how the electric field amplitude increases from deep to shallow water, and they are in quantitative agreement with Figure 8. For offsets 1 to 5 km, the amplitude increases by about one order of magnitude. This is offset by the up to 16 times enhancement of the scattered field due to the combined effects from $G_{zx}^{B^{EJ}}$ and $G_{xz}^{B^{EJ}}$ (see Figure 7) contributing in equation 9. At a longer offset, the increase of background field $G_{xx}^{B^{EJ}}$ dominates and the effect of the airwave can be very large (two orders of magnitude in Figure 1). The total effect on sensitivity upon reducing water depth is therefore nontrivial to assess because it will be enhanced for short offsets and decreased at far offsets. We attribute this behavior to the different offset characteristics of the interactions at the air-water interface for the TE modes contained in the background field $G_{xx}^{B^{EJ}}$ (propagation along the sea surface) and the TM mode (ray-reflected) contributing to the scattered field ΔG_{xx}^{EJ}.

To better define the asymptotic behavior of the airwave and scattered field magnitude, we have in Figure 9 computed the fields for more water depths than shown previously. This plot addresses the dynamics of field amplitude for the water depth interval considered, and it establishes the depth scale where asymptotic behavior is reached.

Let us consider the effect on background field $G_{xx}^{B^{EJ}}$ and scattered field $\Delta G_{xx}^{B^{EJ}}$ upon reducing the water depth from deep water (2000 m) to very shallow water. The background field has an asymptotic amplitude level for water depths larger than 750 m, and at 500 m; that field contribution has increased significantly. The scattered field amplitude is almost constant for water depths

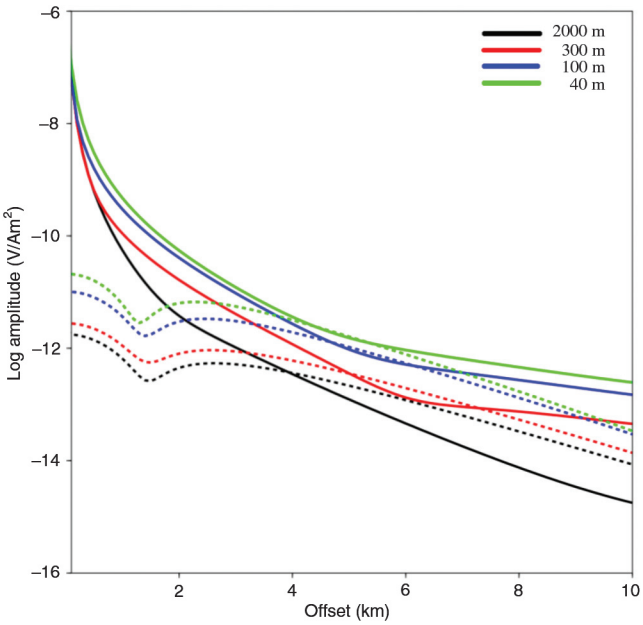

Figure 8. Results of full waveform modeling. Background field contributions as solid lines, and scattered fields as dashed lines.

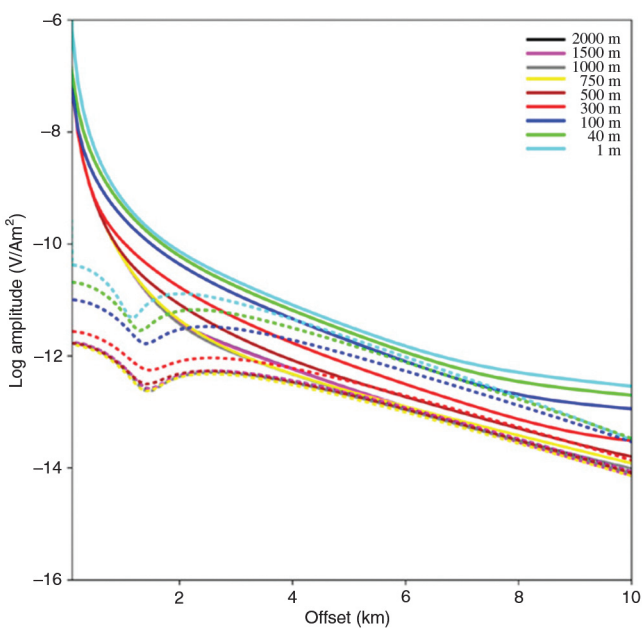

Figure 9. Results of full waveform modeling. Background field and scattered field for many water depths: 2000 m (black), 1500 m (purple), 1000 m (gray), 750 m (yellow), 500 m (brown), 300 m (red), 100 m (blue), 40 m (green), and 1 m (cyan).

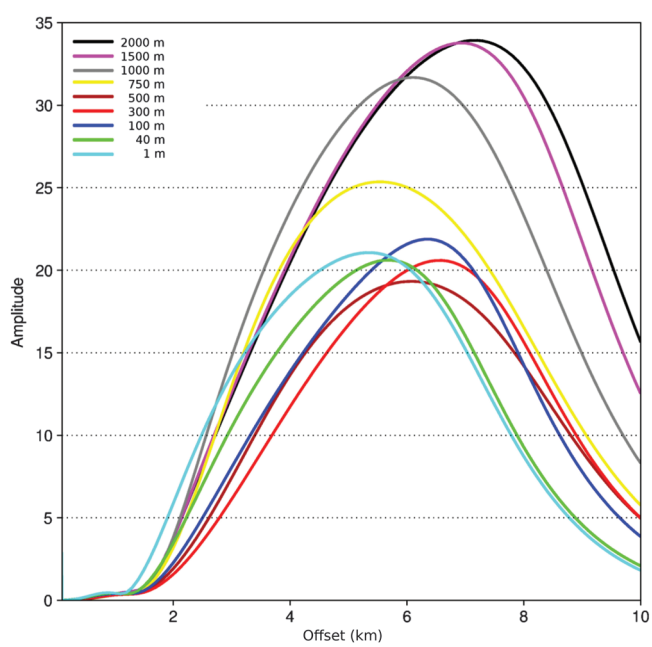

Figure 10. Sensitivity for the range of water depths considered in Figure 9 calculated according to equation 2.

Downloaded 02/11/13 to 62.92.124.145. Redistribution subject to SEG license or copyright; see Terms of Use at http://library.seg.org/

500 m and greater. For shallower water, the scattered field increase discussed in this paper will be important. The resulting sensitivity effect is demonstrated by Figure 10, which considers the scattered field to the data uncertainty according to equation 2 for the same water depths. Decreasing the water depth from 1500 m, there is an associated decrease in sensitivity until 500 m. Then, the increased scattered field response causes the sensitivity to reach a constant level.

Figures 9 and 10 also allow us to consider the limiting case of very shallow water (1 m). Also in this case, the source and receivers were positioned in the water layer. As expected, the sensitivity is similar to that of the 500-m water depth. However, the field amplitudes for the background and scattered field vary considerable even between the 40- and 1-m water depth. The constant level for sensitivity is caused by the corresponding increases of scattered field and background field shown by Figure 9.

CONCLUSIONS

The amplitude of the airwave due to a horizontal electric dipole becomes larger as the water depth is reduced. There is a similar increase in the amplitude of the scattered field from a thin resistor that makes marine CSEM surveys in shallow water feasible. We obtained an approximate but accurate expression for the total field in a shallow-water resistivity model, which includes a thin resistor. This expression determines how the two terms that describe the background field and the scattered field from the thin resistor depend on water depth. The contribution that contain the scattered field is purely TM. The TE mode of the airwave signal, on the other hand, does not couple to the resistive layer and will dominate the background field.

When we analyze the implications for sensitivity of marine CSEM data, we find that the sensitivity is best in deep water, as expected. However, there are only minor differences for data acquired in intermediate water depths of 300 m and shallow water of 40 m.

ACKNOWLEDGMENTS

We thank EMGS ASA for permission to publish this work and M. Zhdanov and three anonymous reviewers who contributed comments that helped us to improve our paper.

APPENDIX A

DERIVATION OF THE THIN RESISTOR RESPONSE

In this appendix, we derive the analytic expression in equation 9, which gives the scattered field from a resistive anomaly. Our starting point is the Lippmann-Schwinger-type equation for the electric and magnetic Green's functions

$$G_{kj}^{EJ}(\mathbf{r}_r|\mathbf{r}_s) = G_{kj}^{B^{EJ}}(\mathbf{r}_r|\mathbf{r}_s) + \int_{V_r} d\mathbf{r} G_{kl}^{B^{EJ}}(\mathbf{r}_r|\mathbf{r})\Delta\sigma_{li}(\mathbf{r})G_{ij}^{EJ}(\mathbf{r}|\mathbf{r}_s), \quad \text{(A-1)}$$

where the Green's function inside the anomalous domain is given by

$$G_{ij}^{EJ}(\mathbf{r}|\mathbf{r}_s) = G_{ij}^{B^{EJ}}(\mathbf{r}|\mathbf{r}_s) + \int_{V_r} d\mathbf{r}' G_{in}^{B^{EJ}}(\mathbf{r}|\mathbf{r}')\Delta\sigma_{nm}(\mathbf{r}')G_{mj}^{EJ}(\mathbf{r}'|\mathbf{r}_s). \quad \text{(A-2)}$$

We seek a simplified expression for the response from a thin resistive layer. The conductivity is assumed isotropic, $\Delta\sigma_{nm} = \Delta\sigma\delta_{nm}$. Anisotropy can change the shallow-water amplitude-gain effect, but not by much compared to what is observed in Figure 4. The electric field due to a horizontal electric dipole transmitter is dominantly vertical within a thin resistive layer. This can easily be verified by full waveform modeling. The physical explanation is that the vertical current must be continuous over the thin resistive layer. This can only happen if the vertical electric field in the thin layer increases discontinuously to counteract the drop in conductivity. The horizontal electric fields are continuous over the same boundaries. We can therefore neglect the contribution due to the horizontal field inside the thin resistive layer. The small parameter involved in this approximation is the ratio of the conductivity of the resistive layer to the conductivity of the formation, σ^r/σ^f. Hence, equation A-2 becomes

$$G_{zx}^{EJ}(\mathbf{r}|\mathbf{r}_s) = G_{zx}^{B^{EJ}}(\mathbf{r}|\mathbf{r}_s) + \int d\mathbf{r}' G_{zz}^{B^{EJ}}(\mathbf{r}|\mathbf{r}')\Delta\sigma(\mathbf{r}')G_{zx}^{EJ}(\mathbf{r}'|\mathbf{r}_s), \quad \text{(A-3)}$$

and for equation A-1 we have

$$G_{xx}^{EJ}(\mathbf{r}_r|\mathbf{r}_s) = G_{xx}^{B^{EJ}}(\mathbf{r}_r|\mathbf{r}_s) + \int d\mathbf{r} G_{xz}^{B^{EJ}}(\mathbf{r}_r|\mathbf{r})\Delta\sigma(\mathbf{r})G_{zx}^{EJ}(\mathbf{r}|\mathbf{r}_s). \quad \text{(A-4)}$$

The derivations to follow are performed in the wavenumber-frequency domain, whereas the plotted results in this paper are displayed in the space-frequency domain. We use $(\mathbf{r}, t) = (\mathbf{r}_h, z, t) = (x, y, z, t)$ for space and time coordinates and $(\mathbf{k}, \omega) = (\mathbf{k}_h, k_z, \omega) = (k_x, k_y, k_z, \omega)$ for wavenumber-frequency coordinates. The square of the horizontal wavenumber is given by $k_h^2 = k_x^2 + k_y^2$. The vertical wavenumber k_z cannot vary freely if the horizontal wavenumbers are allowed to do so. The vertical wavenumber in terms of horizontal wavenumbers and medium parameters will be given below. The following Fourier transform pairs are used:

$$f(\mathbf{k}_h, z, \omega) = \int_{-\infty}^{\infty} d\mathbf{r}_h \int_{-\infty}^{\infty} dt f(\mathbf{r}_h, z, t) e^{-i(\mathbf{k}_h\mathbf{r}_h - \omega t)},$$
$$f(\mathbf{r}_h, z, t) = \frac{1}{(2\pi)^3}\int_{-\infty}^{\infty} d\mathbf{k}_h \int_{-\infty}^{\infty} d\omega f(\mathbf{k}_h, z, \omega) e^{i(\mathbf{k}_h\mathbf{r}_h - \omega t)}. \quad \text{(A-5)}$$

Let ϵ_0 be the electric permittivity of the vacuum with ϵ being the relative permittivity. The conductivity is σ. The complex electric permittivity is then

$$\tilde{\epsilon} = \epsilon\epsilon_0 + i\frac{\sigma}{\omega}. \quad \text{(A-6)}$$

With μ the magnetic permeability, the complex wavenumber is determined by

Downloaded 02/11/13 to 62.92.124.145. Redistribution subject to SEG license or copyright; see Terms of Use at http://library.seg.org/

$$k_\omega^2 = \mu\tilde{\epsilon}\omega^2, \tag{A-7}$$

or, when displacement currents can be neglected,

$$k_\omega^2 \approx i\mu\sigma\omega. \tag{A-8}$$

By convention, we use the positive sign of the vertical wavenumber in the following. Hence, the vertical wavenumber is

$$k_z = k_z(k_h) = \sqrt{k_\omega^2 - k_h^2}. \tag{A-9}$$

The reflection coefficient for one plane wave component is different for the two cases of the electric field being normal to the plane of incidence (TE mode) and the magnetic field being normal to the plane of incidence (TM mode). The reflection coefficients for the horizontal electric field in these two cases can be found from the boundary conditions and are (Stratton, 1941; Kong, 2000; Løseth, 2011)

$$r_{TE}^{ab} = \frac{k_z^a - k_z^b}{k_z^a + k_z^b}, \quad r_{TM}^{ab} = \frac{\tilde{\epsilon}^a k_z^b - \tilde{\epsilon}^b k_z^a}{\tilde{\epsilon}^a k_z^b + \tilde{\epsilon}^b k_z^a}, \tag{A-10}$$

where the superscript a relates to the medium parameters on the side of the interface where we find the incoming and reflected fields and superscript b relates to the medium parameters on the side the interface where we find the transmitted field. The magnetic permeability is assumed constant. As mentioned previously, we use the positive sign of k_z in the coefficients. Seen from the opposite side of the boundary, the reflection coefficients change sign; that is, $r^{ba} = -r^{ab}$. The corresponding transmission coefficients are

$$t_{TE}^{ab} = \frac{2k_z^a}{k_z^a + k_z^b}, \quad t_{TM}^{ab} = \frac{2\tilde{\epsilon}^a k_z^b}{\tilde{\epsilon}^a k_z^b + \tilde{\epsilon}^b k_z^a}. \tag{A-11}$$

This specifies the problem to compute the background electromagnetic fields $G_{zz}^{B^{EJ}}$ and $G_{xz}^{B^{EJ}}$ required in equations A-3 and A-4. We will first consider this computation, and then we derive the Green's function in the model with a thin resistive layer.

The Green's function for an electrical dipole in a uniform whole space can be found, e.g., in Ward and Hohmann (1987). The whole-space conductivity is here denoted σ^a and can be σ^w, σ^f, or σ^r for seawater, formation, or resistor, respectively (see Figure 3). The wavenumber-frequency domain expression can be written as

$$\begin{aligned} G_{ij}^{0,a^{EJ}}(\mathbf{k}_h, z|z') &= F_{ij}^{a^{EJ}}(\mathbf{k}_h) e^{ik_z^a|z-z'|}, \\ G_{ij}^{0,a^{HJ}}(\mathbf{k}_h, z|z') &= F_{ij}^{a^{HJ}}(\mathbf{k}_h) e^{ik_z^a|z-z'|}, \end{aligned} \tag{A-12}$$

where

$$\mathbf{F}^{a^{EJ}}(\mathbf{k}_h) = \frac{1}{\sigma^a} \begin{bmatrix} k_\omega^{a^2} - k_x^2 & -k_x k_y & \pm k_x k_z^a \\ -k_x k_y & k_\omega^{a^2} - k_y^2 & \pm k_y k_z^a \\ \pm k_x k_z^a & \pm k_y k_z^a & k_\omega^{a^2} - k_z^{a^2} \end{bmatrix} \frac{1}{-2ik_z^a}, \tag{A-13}$$

and

$$\mathbf{F}^{a^{HJ}}(\mathbf{k}_h) = \begin{bmatrix} 0 & \mp ik_z^a & ik_y \\ \pm ik_z^a & 0 & -ik_x \\ -ik_y & ik_x & 0 \end{bmatrix} \frac{1}{-2ik_z^a}. \tag{A-14}$$

In equation A-12, we have for convenience split off the phase factors from the whole-space electric and magnetic Green's tensors. The relation between the required components of the background Green's tensor $\mathbf{G}^{B^{EJ}}$ and the corresponding components of the whole-space Green's tensor $\mathbf{G}^{0,a^{EJ}}$ will be derived below.

We are now ready to write equation A-3 in the wavenumber-frequency domain,

$$\begin{aligned} G_{zx}^{EJ}(\mathbf{k}_h, z|z_s) &= G_{zx}^{B^{EJ}}(\mathbf{k}_h, z|z_s) \\ &\quad + \int_{z_1}^{z_2} dz' G_{zz}^{B^{EJ}}(\mathbf{k}_h, z|z')\Delta\sigma(z') G_{zx}^{EJ}(\mathbf{k}_h, z'|z_s), \end{aligned} \tag{A-15}$$

and likewise for equation A-4,

$$\begin{aligned} G_{xx}^{EJ}(\mathbf{k}_h, z_r|z_s) &= G_{xx}^{B^{EJ}}(\mathbf{k}_h, z_r|z_s) \\ &\quad + \int_{z_1}^{z_2} dz G_{xz}^{B^{EJ}}(\mathbf{k}_h, z_r|z)\Delta\sigma(z) G_{zx}^{EJ}(\mathbf{k}_h, z|z_s). \end{aligned} \tag{A-16}$$

Equation A-15 is ambiguous. The background fields in the anomalous domain $G_{zx}^{B^{EJ}}$ and $G_{zz}^{B^{EJ}}$ are not consistently defined yet. The problem relates to the fact that the vertical electric field is discontinuous over the boundary to the anomalous domain. However, the horizontal magnetic fields are continuous over the z_1 and z_2 boundaries. For the magnetic fields, we have

$$\begin{aligned} G_{xx}^{HJ}(\mathbf{k}_h, z|z_s) &= G_{xx}^{B^{HJ}}(\mathbf{k}_h, z|z_s) \\ &\quad + \int_{z_1}^{z_2} dz' G_{xz}^{B^{HJ}}(z|z')\Delta\sigma(z') G_{zx}^{EJ}(\mathbf{k}_h, z'|z_s), \\ G_{yx}^{HJ}(\mathbf{k}_h, z|z_s) &= G_{yx}^{B^{HJ}}(\mathbf{k}_h, z|z_s) \\ &\quad + \int_{z_1}^{z_2} dz' G_{yz}^{B^{HJ}}(z|z')\Delta\sigma(z') G_{zx}^{EJ}(\mathbf{k}_h, z'|z_s). \end{aligned} \tag{A-17}$$

The relation between the electric and magnetic tensor components is governed by Ampere's law, which for the relevant component in the wavenumber domain is

$$\sigma(z) G_{zn}^{EJ}(\mathbf{k}_h, z|z_s) = ik_x G_{yn}^{HJ}(\mathbf{k}_h, z|z_s) - ik_y G_{xn}^{HJ}(\mathbf{k}_h, z|z_s). \tag{A-18}$$

Equation A-18 is valid for the anomalous domain. The conductivity here is denoted σ^r, and it is assumed constant from z_1 to z_2. This gives

Downloaded 02/11/13 to 62.92.124.145. Redistribution subject to SEG license or copyright; see Terms of Use at http://library.seg.org/

$$G_{zx}^{EJ}(\mathbf{k}_h, z|z_s) = \frac{1}{\sigma^r}(ik_x G_{yx}^{B^{HJ}}(\mathbf{k}_h, z|z_s) - ik_y G_{xx}^{B^{HJ}}(\mathbf{k}_h, z|z_s)) + \int_{z_1}^{z_2} dz' \frac{1}{\sigma^r}(ik_x G_{yz}^{B^{HJ}}(\mathbf{k}_h, z|z_s) - ik_y G_{xz}^{B^{HJ}}(\mathbf{k}_h, z|z_s))\Delta\sigma(z') G_{zx}^{EJ}(\mathbf{k}_h, z'|z_s). \tag{A-19}$$

We leave this equation as is for the moment because it is necessary to determine the background Green's tensor components as a function of the whole-space Green's tensor components to proceed.

The background Green's functions for the model shown in Figure 3 all have a similar form. They consist of a whole-space solution multiplied by a reflection series with appropriate phase factors to describe the multiple scattering events in the water layer (Nordskag and Amundsen, 2007; Andréis and MacGregor, 2008). The derivation of the Green's function $G_{xz}^{B^{EJ}}(\mathbf{k}_h, z_r|z)$, required by equation A-16, may serve as an example. The coordinate z is assumed to be at some depth in the formation below the seabed, and the coordinate z_r is assumed to be somewhere in the water layer, not necessarily at the seabed. The background Green's function is then

$$G_{xz}^{B^{EJ}}(\mathbf{k}_h, z_r|z) = G_{xz}^{0,f^{EJ}}(\mathbf{k}_h, z_w|z) t_{TM}^{fw} \{e^{ik_z^w(z_w - z_r)} + r_{TM}^{wa} e^{ik_z^w(z_w + z_r)} + r_{TM}^{wa} r_{TM}^{wf} e^{ik_z^w(z_w - z_r)} e^{i2k_z^w z_w} + \cdots\cdots\cdots\cdots\}, \tag{A-20}$$

where the common factor accounts for the propagation from depth z to the seabed and transmission from the formation to the water layer. Superscript f is for the formation, and superscript w is for the water layer. The sum is a geometric series, and the result is

$$G_{xz}^{B^{EJ}}(\mathbf{k}_h, z_r|z) = G_{xz}^{0,f^{EJ}}(\mathbf{k}_h, z_w|z) t_{TM}^{fw} \left\{ \frac{e^{ik_z^w(z_w - z_r)} + r_{TM}^{wa} e^{ik_z^w(z_w + z_r)}}{1 - r_{TM}^{wa} r_{TM}^{wf} e^{2ik_z^w z_w}} \right\}. \tag{A-21}$$

Note that the above Green's function depends on the inverse of the formation conductivity σ^f because the whole-space Green's function has this dependence. Equation A-21 can also be used for the Green's function $G_{zx}^{B^{EJ}}(\mathbf{k}_h, z|z_s)$, required by equation A-15. Reciprocity dictates that

$$G_{zx}^{B^{EJ}}(\mathbf{k}_h, z|z_s) = G_{xz}^{B^{EJ}}(-\mathbf{k}_h, z_s|z), \tag{A-22}$$

where the right-hand side is given by equation A-21 if z_s is substituted for z_r. For the remaining part of the paper, we assume that the receiver is at the seabed.

The derivation for $G_{xx}^{B^{EJ}}$ is along the same lines as above, except that this Green's function component must be split in its TE and TM modes, $G_{xx_{TE}}^{B^{EJ}}$ and $G_{xx_{TM}}^{B^{EJ}}$. To achieve this, we first need to decompose the amplitudes of the whole-space Green's function in the water layer $F_{xx}^{w^{EJ}}$ in the TE and TM modes (Ward and Hohmann, 1987)

$$F_{xx_{TE}}^{w^{EJ}} = \frac{1}{\sigma^w}\frac{k_y^2 k_\omega^{w^2}}{k_h^2}\left(\frac{1}{-2ik_z^w}\right),$$
$$F_{xx_{TM}}^{w^{EJ}} = \frac{1}{\sigma^w}\frac{k_x^2 k_z^{w^2}}{k_h^2}\left(\frac{1}{-2ik_z^w}\right). \tag{A-23}$$

These amplitudes must be multiplied by the appropriate phase factors, as in equation A-12, to obtain the corresponding whole-space Green's functions $G_{xx_{TE}}^{0,w^{EJ}}$ and $G_{xx_{TM}}^{0,w^{EJ}}$.

We obtain

$$G_{xx_{TE}}^{B^{EJ}}(\mathbf{k}_h, z_r|z_s) = G_{xx_{TE}}^{0,w^{EJ}}(\mathbf{k}_h, z_r|z_s)(1 + r_{TE}^{wf})\frac{1 + e^{2ik_z^w z_s}}{1 - r_{TE}^{wa} r_{TE}^{wf} e^{2ik_z^w z_w}},$$
$$G_{xx_{TM}}^{B^{EJ}}(\mathbf{k}_h, z_r|z_s) = G_{xx_{TM}}^{0,w^{EJ}}(\mathbf{k}_h, z_r|z_s)(1 + r_{TM}^{wf})\frac{1 + e^{2ik_z^w z_s}}{1 - r_{TM}^{wa} r_{TM}^{wf} e^{2ik_z^w z_w}}, \tag{A-24}$$

and

$$G_{xx}^{B^{EJ}}(\mathbf{k}_h, z_r|z_s) = G_{xx_{TE}}^{B^{EJ}}(\mathbf{k}_h, z_r|z_s) + G_{xx_{TM}}^{B^{EJ}}(\mathbf{k}_h, z_r|z_s). \tag{A-25}$$

We can now return to equation A-19. We use equations A-13 and A-14 to obtain an expression that contains only electric Green's functions:

$$G_{zx}^{EJ}(\mathbf{k}_h, z|z_s) = \frac{\sigma^f}{\sigma^r} G_{zx}^{B^{EJ}}(\mathbf{k}_h, z|z_s) + \frac{\sigma^f}{\sigma^r}\int_{z_1}^{z_2} dz' G_{zz}^{B^{EJ}}(\mathbf{k}_h, z|z')\Delta\sigma(z') G_{zx}^{EJ}(\mathbf{k}_h, z'|z_s). \tag{A-26}$$

The next two simplifying assumptions are that the electric fields in the anomalous domain $G_{zx}^{B^{EJ}}$ and $G_{zz}^{B^{EJ}}$ are approximated as constant as a function of depth from z_1 to z_2. The $G_{zx}^{B^{EJ}}$ is assumed slowly varying because the distance from the source depth is fairly large and the resistive layer is thin. The $G_{zz}^{B^{EJ}}$ can be assumed constant because the magnetic fields are continuous over the thin layer and cannot have any jumps over this short depth interval. These approximations require that the thickness of the resistive layer is much smaller than the wavelength of the induced field. With

$$\xi = \frac{\sigma^f}{\sigma^r}, \tag{A-27}$$

we obtain for the anomalous domain,

$$G_{zx}^{EJ}(\mathbf{k}_h, z_1|z_s) = \xi G_{zx}^{B^{EJ}}(\mathbf{k}_h, z_1|z_s) + \xi\Delta\sigma\Delta F_{zz}^{f^{EJ}}(\mathbf{k}_h) G_{zx}^{EJ}(\mathbf{k}_h, z_1|z_s). \tag{A-28}$$

This is now an algebraic equation for the field in the anomalous domain with the solution,

Downloaded 02/11/13 to 62.92.124.145. Redistribution subject to SEG license or copyright; see Terms of Use at http://library.seg.org/

$$G_{zx}^{EJ}(\mathbf{k}_h, z_1|z_s) = \frac{\xi}{1 - \xi\Delta\sigma\Delta z F_{zz}^{f^{EJ}}(k_h)} G_{zx}^{B^{EJ}}(\mathbf{k}_h, z_1|z_s), \tag{A-29}$$

where

$$F_{zz}^{f^{EJ}}(\mathbf{k}_h) = \frac{1}{\sigma^f}\left(\frac{k_h^2}{-2ik_z^f}\right), \tag{A-30}$$

and where we have used $\Delta\sigma = \sigma^r - \sigma^f$ and $\Delta z = z_2 - z_1$. We introduce $\eta = \xi\Delta\sigma\Delta z$, and we obtain for the recorded field at the receiver,

$$\begin{aligned} G_{xx}^{EJ}(\mathbf{k}_h, z_r|z_s) &= G_{xx}^{B^{EJ}}(\mathbf{k}_h, z_r|z_s) + G_{xz}^{B^{EJ}}(\mathbf{k}_h, z_r|z_1) \\ &\quad \times \frac{\eta}{1 - \eta F_{zz}^{f^{EJ}}(\mathbf{k}_h)} G_{zx}^{B^{EJ}}(\mathbf{k}_h, z_1|z_s) \\ &= G_{xx}^{B^{EJ}}(\mathbf{k}_h, z_r|z_s) + \Delta G_{xx}^{EJ}(\mathbf{k}_h, z_r|z_s). \end{aligned} \tag{A-31}$$

The term $G_{xx}^{B^{EJ}}$ captures TE and TM modes of the background airwave signal, whereas $G_{xz}^{B^{EJ}}$ and $G_{zx}^{B^{EJ}}$ are pure TM modes. The scattered field from the resistive anomaly is contained in ΔG_{xx}^{EJ}:

$$\begin{aligned} &\Delta G_{xx}^{EJ}(\mathbf{k}_h, z_r|z_s) \\ &\quad = G_{xz}^{B^{EJ}}(\mathbf{k}_h, z_r|z_1) \frac{\eta}{1 - \eta F_{zz}^{f^{EJ}}(\mathbf{k}_h)} G_{zx}^{B^{EJ}}(\mathbf{k}_h, z_1|z_s). \end{aligned} \tag{A-32}$$

Figure A-1 shows the full waveform modeling result from Figure 4 and also the results from equation A-32 for the model in Figure 3. In Figure A-1, the wavenumber-frequency domain result in equation A-32 has been transformed numerically to the space-frequency domain. The fit is sufficiently good for the discussion in this paper, for all water depths. This means that the approximations used to reach the expression for the scattered field in equation A-32 are valid.

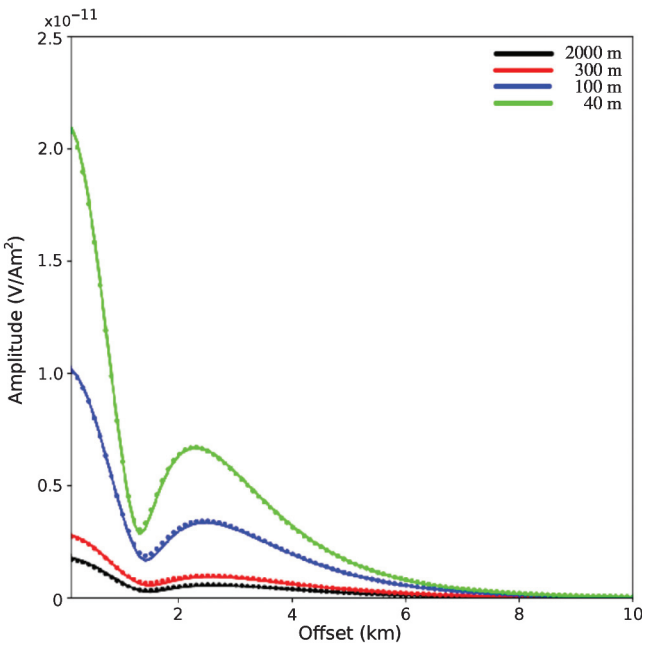

Figure A-1. Absolute value of the scattered fields. The approximate solution in equation A-32 is numerically transformed to the space-frequency domain and is marked with dots. The full waveform plane layer solution is in solid lines. The line colors correspond to different water depths, as shown in the figure key: 2000 m (black), 300 m (red), 100 m (blue), and 40 m (green).

REFERENCES

Amundsen, L., L. O. Løseth, R. Mittet, S. Ellingsrud, and B. Ursin, 2006, Decomposition of electromagnetic fields into upgoing and downgoing components: Geophysics, **71**, no. 5, G211–G223, doi: 10.1190/1.2245468.

Andréis, D., and L. M. MacGregor, 2008, Controlled-source electromagnetic sounding in shallow water: Principles and applications: Geophysics, **73**, no. 1, F21–F32, doi: 10.1190/1.2815721.

Brown, V., M. Hoversten, K. Key, and J. Chen, 2012, Resolution of reservoir scale electrical anisotropy from marine CSEM data: Geophysics, **77**, no. 2, E147–E158, doi: 10.1190/geo2011-0159.1.

Chen, J., and D. Alumbaugh, 2011, Three methods for mitigating airwaves in shallow water marine controlled-source electromagnetic data: Geophysics, **76**, no. 2, F89–F99, doi: 10.1190/1.3536641.

Constable, S., 2010, Ten years of marine CSEM for hydrocarbon exploration: Geophysics, **75**, no. 5, A67–A81, doi: 10.1190/1.3483451.

Constable, S., and C. J. Weiss, 2006, Mapping thin resistors and hydrocarbons with marine EM methods: Insights from 1D modeling: Geophysics, **71**, no. 2, G43–G51, doi: 10.1190/1.2187748.

Cox, C., 1980, Electromagnetic induction in the oceans and inferences on the constitution of the earth: Geophysical Surveys, **4**, 137–156, doi: 10.1007/BF01452963.

Eidesmo, T., S. Ellingsrud, L. M. MacGregor, S. Constable, M. C. Sinha, S. Johansen, F. N. Kong, and H. Westerdahl, 2002, Sea bed logging (SBL), a new method for remote and direct identification of hydrocarbon filled layers in deepwater areas: First Break, **20**, 144–152.

Ellingsrud, S., T. Eidesmo, M. C. Sinha, L. M. MacGregor, and S. Constable, 2002, Remote sensing of hydrocarbon layers by seabed logging (SBL): Results from a cruise offshore Angola: The Leading Edge, **21**, 972–982, doi: 10.1190/1.1518433.

Fanavoll, S., S. Ellingsrud, P. T. Gabrielsen, R. Tharimela, and D. Ridyard, 2012, Exploration with the use of EM data in the Barents Sea: The potential and the challenges: First Break **30**, 89–93.

Hohmann, G. W., 1975, Three-dimensional induced polarization and electromagnetic modeling: Geophysics, **40**, 309–324, doi: 10.1190/1.1440527.

Johansen, S. E., H. E. F. Amundsen, T. Røsten, S. Ellingsrud, T. Eidesmo, and A. H. Bhuyian, 2005, Subsurface hydrocarbons detected by electromagnetic sounding: First Break, **23**, 31–36.

Kong, J. A., 2000, Electromagnetic wave theory: EMW Publishing.

Løseth, L. O., 2011, Insight into the marine controlled-source electromagnetic signal propagation: Geophysical Prospecting, **59**, 145–160, doi: 10.1111/j.1365-2478.2010.00898.x.

Løseth, L. O., and B. Ursin, 2007, Electromagnetic fields in planarly layered anisotropic media: Geophysical Journal International, **170**, 44–80, doi: 10.1111/j.1365-246X.2007.03390.x.

Maaø, F., and A. K. Nguyen, 2010, Enhanced subsurface response for marine CSEM surveying: Geophysics, **75**, no. 3, A7–A10, doi: 10.1190/1.3377054.

Mittet, R., 2008, Normalized amplitude ratios for frequency-domain CSEM in very shallow water: First Break, **26**, 47–54.

Mittet, R., and J. P. Morten, 2012, Detection and imaging sensitivity of the marine CSEM method: Geophysics, **77**, no. 6, E411–E425, doi: 10.1190/geo2012-0016.1.

Nordskag, J. I., and L. Amundsen, 2007, Asymptotic airwave modeling for marine controlled-source electromagnetic surveying: Geophysics, **72**, no. 6, F249–F255, doi: 10.1190/1.2786025.

Stratton, J. A., 1941, Electromagnetic theory: McGraw-Hill.

Ward, S. H., and G. W. Hohmann, 1987, Electromagnetic theory for geophysical applications, *in* M. N. Nabighian, ed., Electromagnetic methods in applied geophysics — Theory: SEG, 131–311.

Weidelt, P., 1975, Electromagnetic induction in three-dimensional structures: Journal of Geophysics, **41**, 85–109.

Young, P., and C. Cox, 1981, Electromagnetic active sounding near the East Pacific Rise: Geophysical Research Letters, **8**, 1043–1046, doi: 10.1029/GL008i010p01043.

Zhdanov, M. S., S. K. Lee, and K. Yoshioka, 2006, Integral equation method for 3D modeling of electromagnetic fields in complex structures with inhomogeneous background conductivity: Geophysics, **71**, no. 6, G333–G345, doi: 10.1190/1.2358403.